



OPEN Nonlinear electronic oscillators as time sensors for high-precision positioning applications

Konstantinos Metaxas¹, Georgia Himona², Alireza Famili⁴, Angelos Stavrou^{3,4}✉ & Yannis Kominis²✉

Precise time measurement is crucial for positioning, navigation and timing applications in modern technology. Nonlinear electronic oscillators supporting self-sustained oscillations are commonly used as clocks in a wide variety of such applications. We propose a high-precision time and position measurement method, based on the phase response of the electronic oscillators and their complex synchronization dynamics under external driving by a received signal. We show that, under well defined conditions for phase-locking, the time delay between two or more signals can be measured, enabling high-precision positioning.

Keywords Positioning, Navigation and timing, Phase-locking, Synchronization, Nonlinear electronic oscillators

Precise time measurement is a crucial factor in almost all technological applications. Historically, the level of technological progress has been strongly correlated with the current precision in time measurement. The problems of the time measurement and the definition of simultaneity emerged at the boundary between science and technology many centuries ago, with the research interest culminating at the turn of the nineteenth to twentieth century, when it became inseparably related to the problem of positioning and the definition of longitude for mapmaking¹. As early as 1898, Poincaré has realized that distant simultaneity has to be defined in a procedural fashion requiring clock synchronization, and that even if two identical oscillators with the same period are utilized, their relative phase cannot be easily controlled². According to the current available technological means, time coordination has been initially achieved by broadcasted signals in pneumatic networks (steam pulses) and electric networks (telegraphic pulses) and, finally, with wireless radio frequency electromagnetic waves. At the dawn of the nineteenth century the pressing demand for precise timing and position has led to intercontinental clock-coordinating cables surrounding the globe, supporting mapmaking observatories and standard railway technology. Moreover, it has placed the problem of timing and simultaneity at the cross section of physics and engineering, playing a crucial role in Einstein's conceptual steps in the construction of the theory of relativity that radically transformed modern physics¹.

This historical relation between timing, positioning and networks strongly persists in modern technological applications where electronic oscillators are used as time sensors and clocks in telecommunication and computer networks, as well as to a vast variety of *Positioning, Navigation and Timing* (PNT) applications^{3–5}.

Today's advanced positioning technologies, such as the Global Navigation Satellite Systems (GNSS), leverage these precise time measurements to provide essential services in navigation and timing. Global Positioning System (GPS), a widely recognized technology, offers global coverage and precise positioning critical for applications ranging from aviation navigation to personal mobile phone location tracking⁶. Despite their widespread utility, satellite-based systems like GPS are susceptible to signal blockage issues in dense urban environments or indoors, which poses significant challenges⁷. To address these limitations, additional technologies such as Wireless Fidelity (Wi-Fi)-based positioning systems⁸ and Inertial Navigation Systems (INS)⁹ have been developed. These systems can operate in environments where GPS signals are weak or unavailable, enhancing location accuracy and reliability. In addition to the aforementioned signal blockage issues, the typical accuracy of satellite-based systems such as GPS (on the order of several meters) renders them unsuitable for a broad range of indoor location-based services. These include applications in emergency response¹⁰, asset tracking¹¹, and autonomous robotic systems¹², as well as emerging technologies such as augmented reality (AR) and virtual reality (VR)¹³,

¹School of Electrical and Computer Engineering, National Technical University of Athens, 15780 Athens, Greece.

²School of Applied Mathematical and Physical Science, National Technical University of Athens, 15780 Athens, Greece. ³Department of Electrical and Computer Engineering, Virginia Tech, Arlington, VA 22203, USA. ⁴WayWave Inc., Arlington, VA 22203, USA. ✉email: angelos@vt.edu; gkomin@central.ntua.gr

which demand sub-centimeter precision. Although vision-based methods can achieve high accuracy, they are hindered by poor performance in low-light or dark environments and entail significant computational overhead¹⁴. Meanwhile, ranging-based techniques, which depend on the transmission and reception of RF or acoustic signals, suffer from accuracy degradation due to noise accumulation, signal fading, and constraints imposed by receiver bandwidth^{7,12}. The integration of multiple positioning technologies into a hybrid approach, often involving sensors like accelerometers and gyroscopes, helps to mitigate the limitations of each system but introduces complexity and increases resource demands¹⁵.

Synchronized nonlinear electronic oscillators have been traditionally employed in telecommunication applications, functioning as frequency dividers or radio-frequency transceivers^{16–18}. State-of-the-art synchronization techniques of electronic oscillators are commonly based on phase-locked loops (PLL) or direct injection locking (DIL) techniques. PLLs operation mechanism requires an active feedback loop using a phase detector, loop filter, and a voltage-controlled oscillator, and is more complex, requiring multiple components and careful design, in comparison to DIL. Moreover, PLLs are, in general, more tunable, but also more power consuming and have a slower locking time than IDL-based systems. Injection locking techniques have been mostly studied in the frequency domain with time-averaging in combination with Slowly Varying Amplitude^{17–19} or Phase-reduced models^{16,20–22}, being the main tools to study locking phenomena and determine approximately the resonance regions of almost harmonic oscillators. Although the key concepts of circle maps²³, isochrons^{24,25} and devil's staircase²⁶, have been introduced in this field, a time-domain approach that leverages the dynamical complexity of synchronization, as already established in photonics^{27,28}, for precise time measurement and positioning applications^{29–31} has yet to be employed.

In this work, we propose a mechanism, exploiting the dynamical properties of nonlinear electronic oscillators that determine their response to external stimulations, in order to measure the time delay between signals arriving at oscillators anchored in different spatial positions. In the case of a signal broadcasted from an object with unknown location, the relative time delays between the anchored oscillators can be used for its accurate positioning, without necessitating any other common reference. Our study takes advantage of advanced mathematical methods for the study of complex synchronization dynamics and phase-locking, originally used in the context of mathematical biology (e.g. heart pacemakers)^{32,33} and computational neuroscience^{34–36}. Our time-domain approach has the significant advantage that can be applied to any type of input signal and oscillator, either harmonic or highly non-harmonic, resulting on the simultaneous synchronization of all frequency components. Moreover, the nonlinear character of the driven oscillator dynamics ensures exponentially fast convergence to phase-locking and robustness.

This paper is organized as follows: First, we review the basic dynamical concepts and properties of nonlinear electronic oscillators using two fundamental models, the Hopf and the Van der Pol oscillators. Next, we examine the complex synchronization dynamics of limit-cycle electronic oscillators through a reduced phase model. Following that, we present the mechanism for measuring the time delay between the arrival of a broadcasted signal at oscillators in different spatial positions, using a realistic model of a standard Colpitts oscillator to demonstrate precise positioning based on differential time of arrival. Finally, we summarize the main conclusions.

Isochrons and phase response of electronic limit cycle oscillators

Limit cycles and isochrons

Electronic circuits serving as clocks support self-sustained oscillations and correspond to dynamical systems possessing stable *limit cycles*^{37,38}. The periods of the limit cycles are determined by the specific parameter values of the underlying model and their stability implies that, under any finite-time perturbation, the system will finally relax exponentially on its oscillatory state.

An archetypal mathematical model of a limit-cycle oscillator is the well-known Hopf oscillator, which can locally represent a large class of oscillators as their normal form given in polar coordinates³⁹

$$\begin{aligned}\dot{r} &= \lambda r(1 - r^2) \\ \dot{\phi} &= \omega\end{aligned}\quad (1)$$

The system has an unstable fixed point at the origin ($r = 0$) and a limit cycle of unit radius ($r = 1$) which is stable when $\lambda > 0$. The magnitude of λ determines the convergence rate of initial conditions or perturbations to the stable limit cycle and ω is the frequency of the oscillatory state.

The most popular simple model for an electronic circuit supporting stable limit cycles is the Van der Pol oscillator

$$\begin{aligned}\dot{x} &= y \\ \dot{y} &= \mu(1 - x^2)y - x\end{aligned}\quad (2)$$

with μ being a parameter indicating the nonlinear damping of the system⁴⁰. The Van der Pol oscillator, when operated at parameter values suggesting the existence of a stable limit cycle, has qualitatively similar dynamical properties with the Hopf oscillator and can be implemented by various electronic circuits.

The shapes of the limit cycles in the state spaces of the two oscillators are depicted in Fig. 1a, b. Apart from its specific shape, characteristic frequency and convergence rate, a limit cycle is characterized by its accompanying *isochrons'* structure that crucially determine the response of the system to external perturbations and, therefore, its synchronization with periodic inputs.

As the system evolves along a limit cycle, the phase of the oscillation $\theta \in [0, 2\pi)$ can be readily defined, with an arbitrarily chosen point of zero phase. For every point within the basin of attraction of a stable limit cycle (i.e.

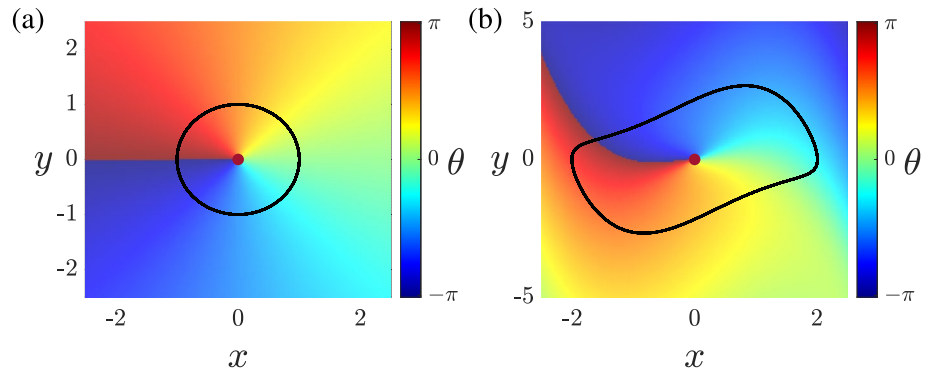


Fig. 1. (a) Isochrons of Hopf oscillator in the Cartesian coordinate system (parameter values: $\lambda = 1, \omega = 1$); (b) isochrons of Van der Pol oscillator (parameter value: $\mu = 1$).

the subset of the state space where initial conditions converge to the limit cycle), we can extend the definition of the phase by assigning an *asymptotic phase*, that is the relative phase of the asymptotic solution after the transient time required for converging to the limit cycle, corresponding to this initial condition. Isochrons correspond to curves consisting of points with the same asymptotic phase, and they partition the entire basin of attraction of the limit cycle^{32,41}. The structure of the isochrons in the state space is shown in Fig. 1a, b for the Hopf and the Van der Pol oscillators. The complement set of the basin of attraction in the state space is the *phaseless set*, which consists solely of the origin in the cases depicted in Fig. 1. The structure of the isochrons is characteristic for each oscillator and it is determined by the form of the limit cycle and the phaseless set. Based on these structures, the Hopf oscillator is referred to as a *radial isochron clock*, whereas the Van der Pol oscillator can be referred to as a *general radial isochron clock*, due to the curved form of its isochrons⁴².

Phase response and time sensing

The isochrons' structure crucially determines the response of the system under an external stimulus. The application of a pulsed perturbation to a system oscillating along a limit cycle moves the state of the system to a new point in the state space. Since this point lies within the basin of attraction, it belongs to a specific isochron that determines the asymptotic phase of the oscillation after relaxation of the system to the stable limit cycle. The effect of the pulsed perturbation is a phase advance or delay with respect to the absence of perturbation. The *Phase Transition Curve* (PTC) and the *Phase Response Curve* (PRC) for a given perturbation strength A are defined, respectively, as the new phase θ' and the phase difference before and after a perturbing pulse, which is applied when the oscillation phase is θ :

$$\text{PTC}(\theta) = \theta' \tag{3}$$

$$\text{PRC}(\theta) = \theta' - \theta. \tag{4}$$

The PTC and the PRC can be readily calculated either numerically or experimentally, by repeated measurements of the new phase of the oscillation after the application of the stimulating pulse at different phases of the oscillation. It is worth emphasizing that in the case of experimental measurement, there is no need for a specific mathematical model, and the method of phase reduction for the study of synchronization dynamics can be applied with the utilization of the experimentally obtained curves, therefore facilitating the consideration of any system. For the simplest Hopf oscillator model (1), the asymptotic phase function θ can be readily obtained analytically and expressed as

$$\theta(r, \phi) = \phi. \tag{5}$$

PRCs can be calculated analytically for arbitrary stimulation amplitudes. For the case of a stimulus in the form of a Dirac delta function, depending on whether the stimulus perturbs the system along the x or y Cartesian direction, the PRC can be defined as a two-component vector

$$\text{PRC}(\theta, A) = (\text{PRC}_x(\theta, A), \text{PRC}_y(\theta, A)),$$

with

$$\begin{aligned} \text{PRC}_x(\theta, A) &= (-1)^{\lceil 1 - \sin \theta / 2 \rceil} \arccos \left(\frac{1 + A \cos \theta}{\sqrt{1 + 2A \cos \theta + A^2}} \right), \\ \text{PRC}_y(\theta, A) &= (-1)^{\lceil \cos \theta / 2 - 1 \rceil} \arccos \left(\frac{1 + A \sin \theta}{\sqrt{1 + 2A \sin \theta + A^2}} \right), \end{aligned}$$

where $\lceil \cdot \rceil$ denotes the ceiling function. PRCs/PTCs defined also as functions of the amplitude are referred to as *generalized PRCs/PTCs*.

Depending on the amplitude A of the stimulation in comparison to the radius of the limit cycle ($r = 1$) two qualitatively different types can be distinguished³⁴: Type 1, for relatively weak amplitudes ($A < 1$), resulting in continuous PRCs and monotonic PTCs with mean slope equal to one (Figs. 2a–c); Type 0, for relatively strong amplitudes ($A > 1$), resulting in discontinuous PRCs and non-monotonic PTCs with mean slope equal to zero (Fig. 2d–f). It is worth noting that these qualitative characteristics of the phase response of the simple Hopf oscillator under a Dirac delta function stimulation are typical for all types of limit cycle oscillators, stimulated by pulses of finite duration having arbitrary forms, as will also be shown in a following section for the case of a realistic Colpitts oscillator perturbed by a rectangular pulse.

The phase response of a limit-cycle oscillator can be considered as the response function of a *time sensor*, according to which the occurrence time (clock phase θ) of an event (pulse) can be determined by the phase advancement or delay (new phase θ') of the clock, especially for the case of a one-to-one correspondence suggested by a monotonic PTC of Type 1.

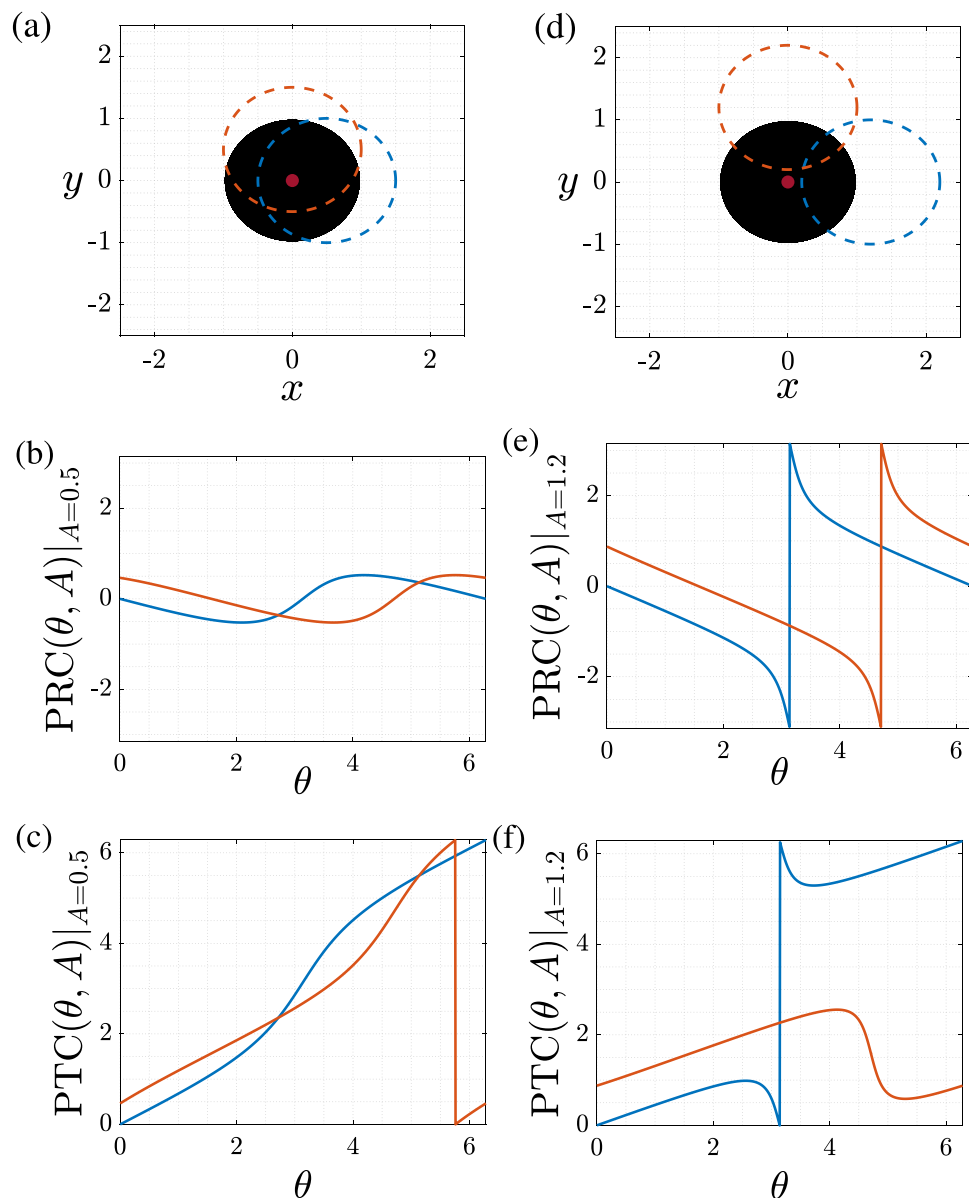


Fig. 2. Limit cycle of the Hopf oscillator ($\lambda = 1$, $\omega = 1$) perturbed along the x (blue curves) and the y (red curves) directions, along with the corresponding PRCs and PTCs. The magnitude of the stimulus A in comparison to the radius of the limit cycle ($r = 1$) differentiates the form of the PRCs and the PTCs. Small amplitudes ($A = 0.5$) result in continuous PRCs and monotonic PTCs as depicted in (a–c); large amplitudes ($A = 1.2$) result in discontinuous PRCs and non-monotonic PTCs as depicted in (d–f).

Phase reduction and complex synchronization dynamics of periodically driven electronic oscillators

A periodic sequence of pulsatile stimulations can lock an electronic oscillator to a constant phase with respect to it (similarly to the operation of a heart pacemaker), or even drive the oscillator to a chaotic state^{34,43}. The phase response of the cycle oscillator, as described by the PRC/PTC function obtained for a single pulsatile stimulation, can be used for the study of its synchronization dynamics with a periodic input consisting of equidistant identical pulses. The period of the pulse sequence can be written as $T_{in} = (k + s)T$, $k \in \mathbb{N}$, $s \in [0, 1)$, where T is the period of the unforced limit cycle. Under the assumption that the period of the incoming pulse sequence is large enough for the oscillator to relax on the stable limit cycle within the time interval between two subsequent pulses (i.e. a sufficiently large value of k), the complex synchronization dynamics can be accurately described in terms of a one-dimensional (Poincaré) circle map:

$$\theta_{n+1} = \theta_n + \text{PRC}(\theta_n, A) + 2\pi s \pmod{2\pi}, \quad (6)$$

where θ_n is the oscillation phase before the n -th stimulus. This drastic dimensional reduction is described as *phase reduction*^{32,34,43} and can be performed solely on the basis of a numerically or experimentally obtained PRC, facilitating the application of the respective analysis to realistic (even model free) configurations.

The seemingly simple circle map of Eq. (6) has a remarkably rich set of dynamical features. Phase locking with respect to the periodic pulse sequence corresponds to fixed points of the map given from the equation

$$\text{PRC}(\theta_n, A) = 2\pi(1 - s) \quad (7)$$

providing the synchronization conditions for which the stimulated phase shift compensates for the difference of the two periods (detuning). The amplitude of the PRC determines the margin for the detuning in order to achieve synchronization, and its slope determines the stability of the fixed point and the corresponding synchronized state as

$$-2 < \text{PRC}'(\theta, A) < 0, \quad (8)$$

where prime denotes differentiation with respect to θ . The form of the generalized PRC/PTC, determining the synchronization properties of the reduced circle map and the original system, for a Hopf and a Van der Pol oscillator are depicted in Fig. 3a,b and d,e, respectively, with the generalized PTC also known as the *time crystal* of the limit-cycle oscillator³².

The minimum dimension and the simplicity of the circle map facilitates the systematic numerical investigation of the synchronization properties of the system in the parameter space of the periodic pulse sequence in a remarkably computationally efficient fashion. The rotation number ρ expresses the average increase in the phase θ per iteration and is defined as

$$\rho = \lim_{n \rightarrow \infty} \frac{\Theta_n - \Theta_t}{n - t} \quad (9)$$

where Θ is the lift of the asymptotic phase function θ to the real axis, and t denotes a number of excluded initial (transient) iterations. A zero value of the rotational number ($\rho = 0$) indicates a one-to-one phase locking with the periodic pulse sequence, where the frequency of the oscillator precisely matches that of the external force. In contrast, non-zero rational values of the rotation number ($\rho = p/q \in \mathbb{Q}$) correspond to higher-order synchronization. Here p denotes the number of cycles completed by the oscillator, while q denotes the number of cycles of the external force. The resonance diagrams, depicting the rotation number as a function of the forcing parameters s and the pulse amplitude, for the Hopf and the Van der Pol oscillators are depicted in Fig. 3c,f, respectively. The phase-locking regions emanate from rational points of the horizontal (zero amplitude) axis and form the well-known Arnold tongues^{44,45}. The dynamics within the Arnold tongues as well as the bifurcations taking place at their boundaries depend crucially on the forcing amplitude determining whether it corresponds to Type-1 or Type-0 stimulation. For relatively small amplitudes, the dynamics are uniquely determined by the rotation number, whereas for larger amplitudes bifurcations leading to chaotic evolution may take place without any change in the rotation number⁴⁶.

Time delay measurement based on synchronization dynamics of a driven Colpitts oscillator

As discussed in the previous sections, the phase locking of an electronic limit-cycle oscillator to an external periodic pulse sequence is a complex process that depends crucially on the parameters of the free-running oscillator (PRC/PTC) as well as on the characteristics of the external signal. In this section we apply the method of phase reduction to one of the most popular and widely used electronic oscillators, namely the Colpitts oscillator. The robustness of the method is demonstrated by the utilization of a differential equation model of the system, as well as a Simulink⁴⁷ model with non-ideal parameters resembling an experimental set up. Our aim is to determine phase-locking conditions that will be used for the operation of two (or more) Colpitts oscillators acted upon by the same periodic pulse sequence emitted by the same source and arrived at each one of them at different time moments due to different distances from the source. In that case, all oscillators are phase locked to the incoming periodic signal but with a relative phase delay that is proportional to their differential distance from the source, allowing for precise positioning of the broadcasting object.

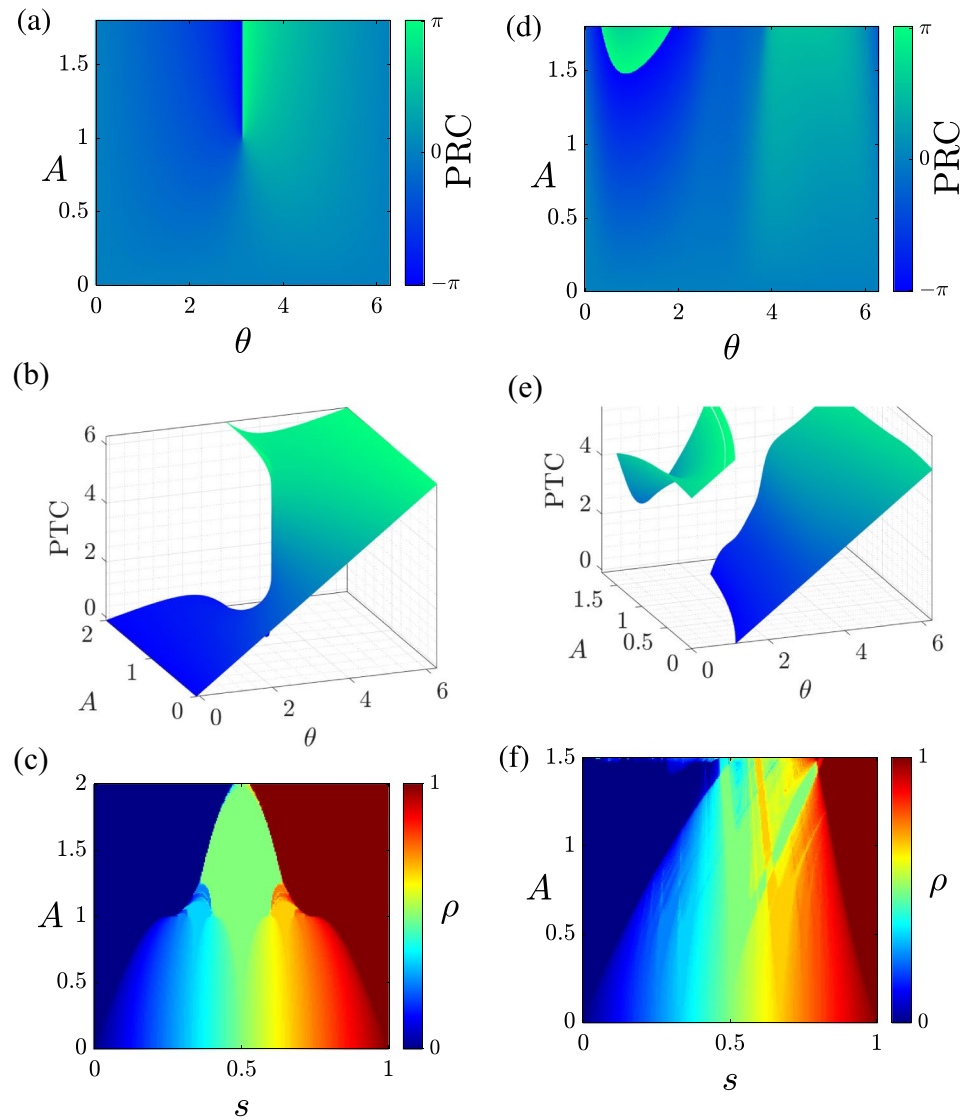


Fig. 3. (a) Generalized PRC, (b) generalized PTC (time crystal), and (c) resonance diagram of Hopf oscillator ($\lambda = 1, \omega = 1$). (d) Generalized PRC, (e) generalized PTC (time crystal), and (f) resonance diagram of Van der Pol oscillator ($\mu = 1$).

The Colpitts oscillator, depicted in Fig. 4, is described by the nonlinear system of differential equations^{48,49}

$$\begin{aligned} \dot{x} &= \frac{g}{Q(1-K)} (1 - e^{-y} + z) \\ \dot{y} &= \frac{g}{QK} (z + Af(t)) \\ \dot{z} &= -\frac{QK(1-K)}{g} (x + y) - \frac{1}{Q}z, \end{aligned} \tag{10}$$

where A is the normalized amplitude of a time dependent current source $i(t) = Af(t)$ connected in parallel with the current source I . The resistor R accounts for the ohmic losses of the inductor (all other elements are assumed ideal). The parameters K, Q, g in terms of the circuit elements are given by^{48,49}

$$K = \frac{C_1}{C_1 + C_2}, \quad Q = \sqrt{\frac{L(C_1 + C_2)}{RC_1C_2}}, \quad g = \frac{IL}{V_T R(C_1 + C_2)}, \tag{11}$$

and the state variables are normalized voltages and current, respectively, expressed as^{48,49},

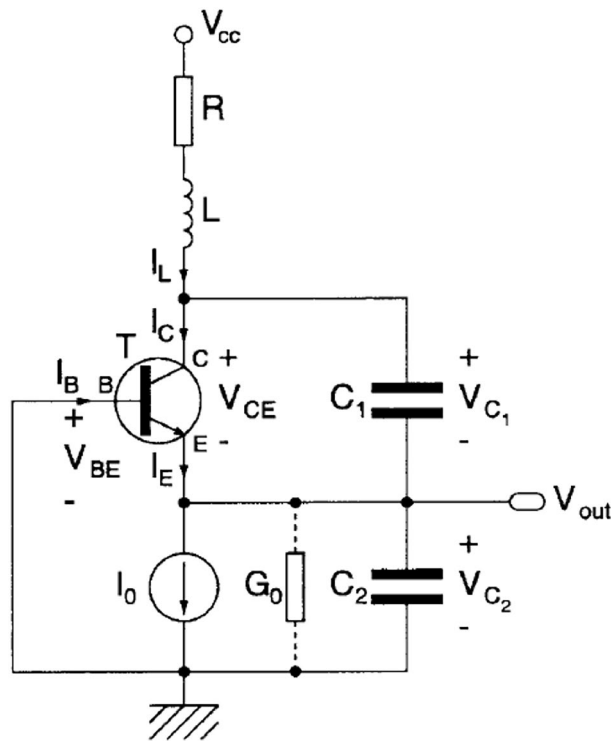


Figure 4. Schematic of the Colpitts oscillator^{48,49}.

$$\begin{aligned}
 x &= \frac{v_{C1} - v_{C1,eq}}{V_T} \\
 y &= \frac{v_{C2} - v_{C2,eq}}{V_T} \\
 z &= \frac{i_L - i_{L,eq}}{I}
 \end{aligned}
 \tag{12}$$

where

$$\begin{aligned}
 v_{C1,eq} &= V_{cc} - RI - V_T \ln\left(\frac{I_s}{I}\right) \\
 v_{C2,eq} &= V_T \ln\left(\frac{I_s}{I}\right) \\
 i_{L,eq} &= I.
 \end{aligned}
 \tag{13}$$

In the following we assume that $f(t)$ in Eqs. (10) has the form of a periodic sequence of rectangular pulses,

$$f(t) = \sum_{n=0}^{\infty} \mathbb{1}_{[0, T_{on})}(t - nT_{in}),
 \tag{14}$$

where $\mathbb{1}_{[0, T_{on})}$ denotes the rectangular pulse function of unitary amplitude and duration T_{on} . We consider a pulse width of $T_{on} = T/10$ and a period $T_{in} = (k + s)T$, $k \in \mathbb{N}$, $s \in [0, 1)$, where T is the period of the unforced limit cycle. The parameters of the circuit are given in Table 1 and the transistor's in Table 2. We remark that although Eqs.(10) refers to an ideal Colpitts oscillator, the respective Simulink model takes into account system's nonidealities.

Phase response and synchronization dynamics of the Colpitts oscillator

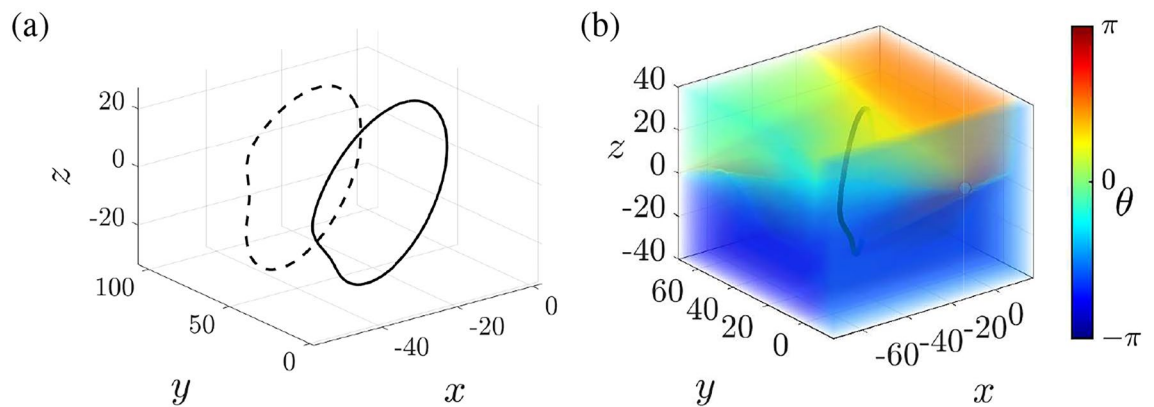
The stable limit cycle of the Colpitts oscillator for a set of parameter values $\log_{10} g = 1.18$, $\log_{10} Q = 1.44$, $K = 0.5$ has a period of $T = 1.37 \mu s$ and is depicted in Fig. 5a along with the perturbed initial conditions after the action of a single rectangular pulse with amplitude $A = 75$. The isochrons span the basin of attraction of the stable limit cycle consisting of the entire three-dimensional state space except from the unstable fixed point at the origin, as shown in Fig. 5b. Their computation has been performed with the utilization of *Fourier averages*^{50–52} evaluated on trajectories of the continuous-time ideal system (10).

The structure of the isochrons in the state space determines the phase response of the oscillator as fully described by the generalized PRC and PTC shown in Fig. 6a, d. Characteristic PRCs and PTCs for moderate

Element-parameter	Value	Nonideality
Resistor R	20Ω	Tolerance $\pm 1\%$
Inductor L	0.12 mH	Ohmic losses: R
Capacitors $C_1 = C_2$	0.8 nF	Series resistance: $10^{-8} \Omega$
Current source I	0.1 mA	Finite parallel conductance
Parameter $\log_{10} g$	1.18	Inherited
Parameter $\log_{10} Q$	1.44	Inherited
Parameter K	0.5	-

Table 1. Circuit elements and nonidealities.

Transistor's parameters	Value	Nonideality
Saturation current I_s	10^{-14} A	-
Forward current transfer β	100	Finite value
Forward early voltage	200 V	Finite value
Base and emitter resistors	$10^{-4} \Omega$	Non-zero value
Parasitic capacitors ¹	0.1 fF	Non-zero value

Table 2. Transistor's parameters and nonidealities. ¹Since they are in parallel with $C_{1,2}$, their influence is mostly negligible**Fig. 5.** (a) Unperturbed (solid) and perturbed (dashed) limit cycle after one pulse with amplitude $A = 75$. (b) Isochrons. Parameter values $\log_{10} g = 1.18$, $\log_{10} Q = 1.44$, $K = 0.5$.

($A = 75$) and strong ($A = 97$) forcing are depicted in Fig. 6b, e. In the case where ($A = 75$), the Phase Response Curve (PRC) is continuous, and the Phase Transition Curve (PTC) is monotonic, preserving the orientation of the mapping and thus corresponds to a Type 0 curve. However, orientation is not preserved in the case of strong forcing, corresponding to a Type 1 curve. The PRCs and PTCs as calculated from the mathematical model given by Eq. (10) and the Simulink model are compared and shown in agreement in Fig. 6c, f. It is worth noting that even the small discrepancies between the two curves do not actually compromise the application of the phase reduction method, since either one of them can be used for the study of the synchronization dynamics and the phase-locking conditions; calculations based on Eq. (10), as less computational time-consuming, can be used as a very accurate approximation for identifying the phase-locking regions in extended parameter scans, and the more realistic and time consuming calculations based on the Simulink (or other realistic) model can be used, when focusing in a specific region of resonance diagram.

The resonance diagram with the characteristic Arnold tongues is depicted in Fig. 7a. The rotation number as a function of s for a given forcing amplitude A has the characteristic form of a “Devil’s staircase”^{26,37}, as shown in Fig. 7b with the regions of s with a constant rational value corresponding to the various orders of phase-locking. We remark that the difference between Type 0 and Type 1 curves manifests in the Devil’s staircase as ρ not being increasing with respect to s . (c.f. 7(b,c)).

Time delay measurements and positioning accuracy

The proposed positioning scheme is based on the calculation of the time difference of arrival (TDOA) of a periodic signal emitted by a source and received by a number of modules (oscillators) located at different

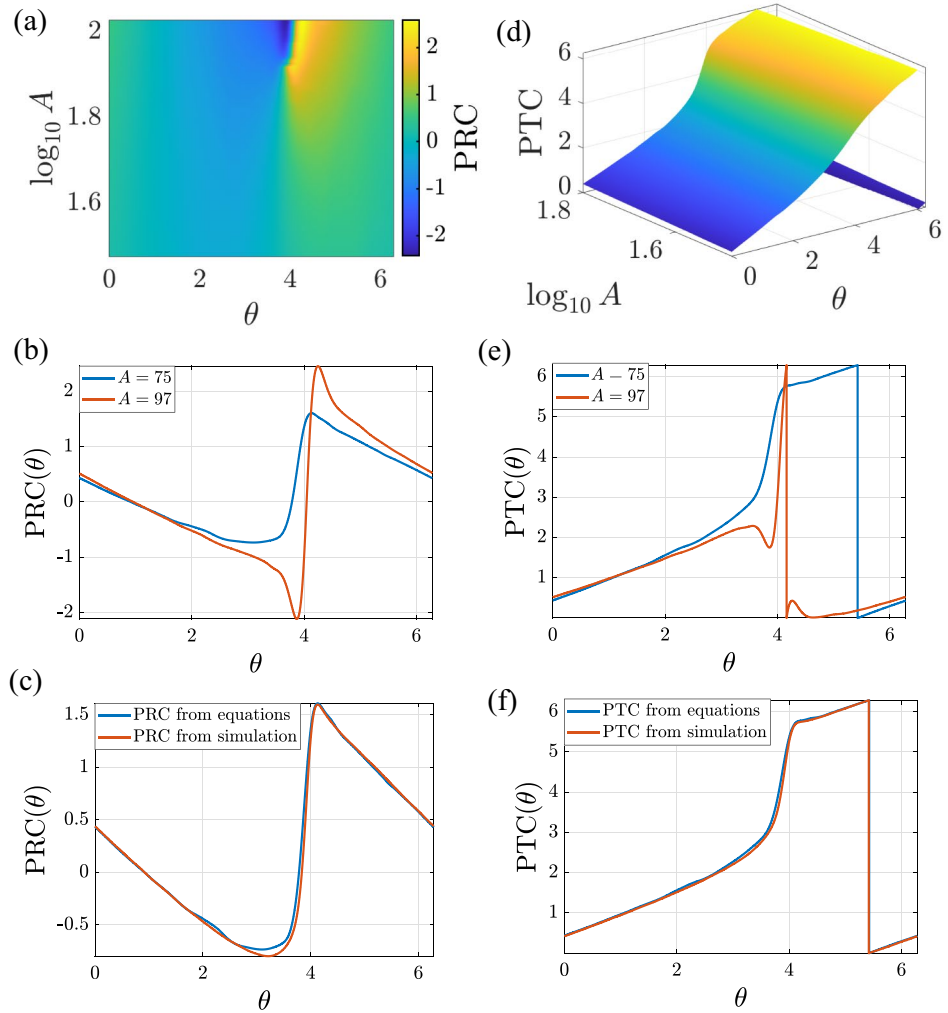


Fig. 6. PRC and PTC curves for parameter values $\log_{10} g = 1.18$, $\log_{10} Q = 1.44$, $K = 0.5$. **(a)** Generalized PRC, **(d)** generalized PTC (time crystal). **(b,e)** PRCs and PTCs for weak and strong forcing. **(c,f)** PRC and PTC for $A = 75$ as obtained from the mathematical model given by Eq. (10) and via Simulink simulations.

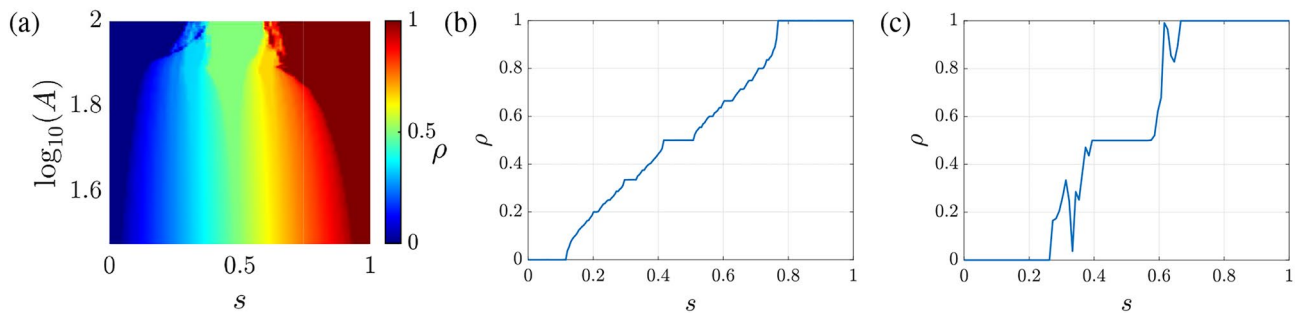


Fig. 7. **(a)** Resonance diagram for the Colpitts oscillator. **(b,c)** Devil's staircase for moderate ($A = 75$, type 0 PRC) and strong ($A = 97$, type 1 PRC) forcing. The rotation number $\rho(s; A)$ is not continuously increasing for Type 1 curves. Parameter values $\log_{10} g = 1.18$, $\log_{10} Q = 1.44$, $K = 0.5$.

positions. The incoming periodic pulse sequence can either be directly injected, or trigger a secondary pulse sequence with prescribed amplitude that is injected to each oscillator. In the second case, only the information of the relative time of arrival is kept in the injected signal that is cleared from possible distortion and/or fading due to the wireless propagation channel. The characteristic features of the measuring mechanism can be essentially

described by the synchronization dynamics of two Colpitts oscillators acted upon by the same periodic signal injected in each oscillator with a relative time delay due to different distance from the source. Under appropriate conditions ensuring phase-locking, the two oscillators have the same phase difference with respect to their incoming periodic signals, so that the comparison of their relative phases directly provides the *differential time of arrival* between the two incoming signals, and therefore the respective differential distance. The block diagram of the simulation setup is illustrated in Fig. 8.

Based on the resonance diagram in Fig. 7, we select the perturbation parameters $s = 0.1$ and $A = 75$, which lie within the 1 : 1 resonant Arnold tongue. We perturb two identical Colpitts oscillators using the forcing described in Eq. (14) with $k = 60$. The synchronization dynamics can be studied by iterating the one-dimensional circle map of Eq. (6) with the utilization of the calculated PRC of Fig. 6c. The exponential convergence to the stable fixed point of the circle map corresponding to the phase-locked state is depicted in Fig. 9a, b. The location of the stable fixed point corresponding to the final constant phase difference with respect to the incoming periodic signal is shown in Fig. 9c. In order to confirm that the circle map provides the right conditions for phase-locking for the original three dimensional system, the output spectrum of the system variable $x(t)$ is depicted in Fig. 9d. The discrete spectrum is shown to consist of equidistant spectral lines with a spacing equal to $1/(k + s)T$ confirming the periodicity of the output and the phase-locking of the original system. It is worth noting that the differences in calculations based on Eq. (10) and the Simulink model, in the diagrams depicted in Figs. 7 and 9, are hardly visible.

Under these phase-locking conditions the relative time delay Δt between the two oscillators can be readily measured, as shown in Fig. 10, to calculate the relative distance $\Delta d \equiv d_2 - d_1 = c\Delta t$, where c is the speed of light. To measure the time delay, we use an ideal bandpass filter with a central frequency equal to the frequency of the locked oscillators, namely $1/(k + s)T$, which extracts the Fourier coefficient at this harmonic. The difference between the arguments of the coefficients of the two synchronized oscillators corresponds to the desired phase difference, which is then converted to the relative time delay. It is worth emphasizing that, due to the synchronization in the time-domain, all spectral components of the output signals have the same phase difference. This feature results in relaxed requirements for the characteristics of the bandpass filter and the exact matching of its central frequency with values depending on circuit elements, that may not be ideal. Table 3 shows the errors in estimating the time delay and relative distance across ten measurements, using random ground truth values. The sources of the small reported errors are primarily due to finite numerical accuracy and deviations in parameter values resulting from nonidealities. Another source of error is due to the finite time of the time-delay measurement. Theoretically, an infinite time is required, since the circle map converges asymptotically to the fixed point corresponding to the phase-locking state. However, this convergence is exponential, as also shown in Fig. 9(a), so that the error decreases rapidly for increasing time interval of measurement and its practical importance is negligible. In the simulation, we use only a finite time interval of NT_{in} , with $N = 35$ and let the oscillators evolve autonomously. Finally, a theoretical source of error is related to the relative tolerance of the order 10^{-10} used in the numerical calculations. The time interval required for phase-locking determines the update rate of the position calculation $T_{up} = N(k + s)T$, which has the value of $2.89ms$ for the specific parameter values. It is worth noting that the required values for k and N , determining T_{up} , depend on the exponential convergence rates of a perturbed initial conditions to the limit cycle and the convergence to the fixed point of the circle map, respectively. These values can be further reduced drastically by optimizing with respect to the selection of the parameters of the oscillator determining the period and the convergence rate to the stable limit cycle as well as the selection of the stable phase-locked state. The robustness of the stable limit-cycle free-running oscillations along with the stability of the phase-locking dynamics of each oscillator to an input that differs only in a finite time delay, suggests robustness of the timing mechanism

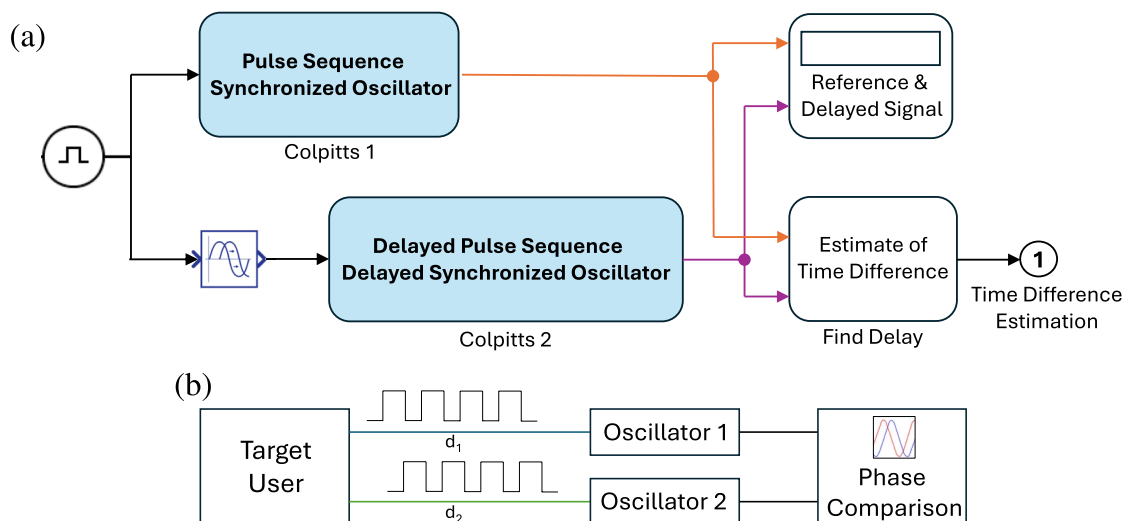


Fig. 8. Block diagram of the time delay measurement setup.

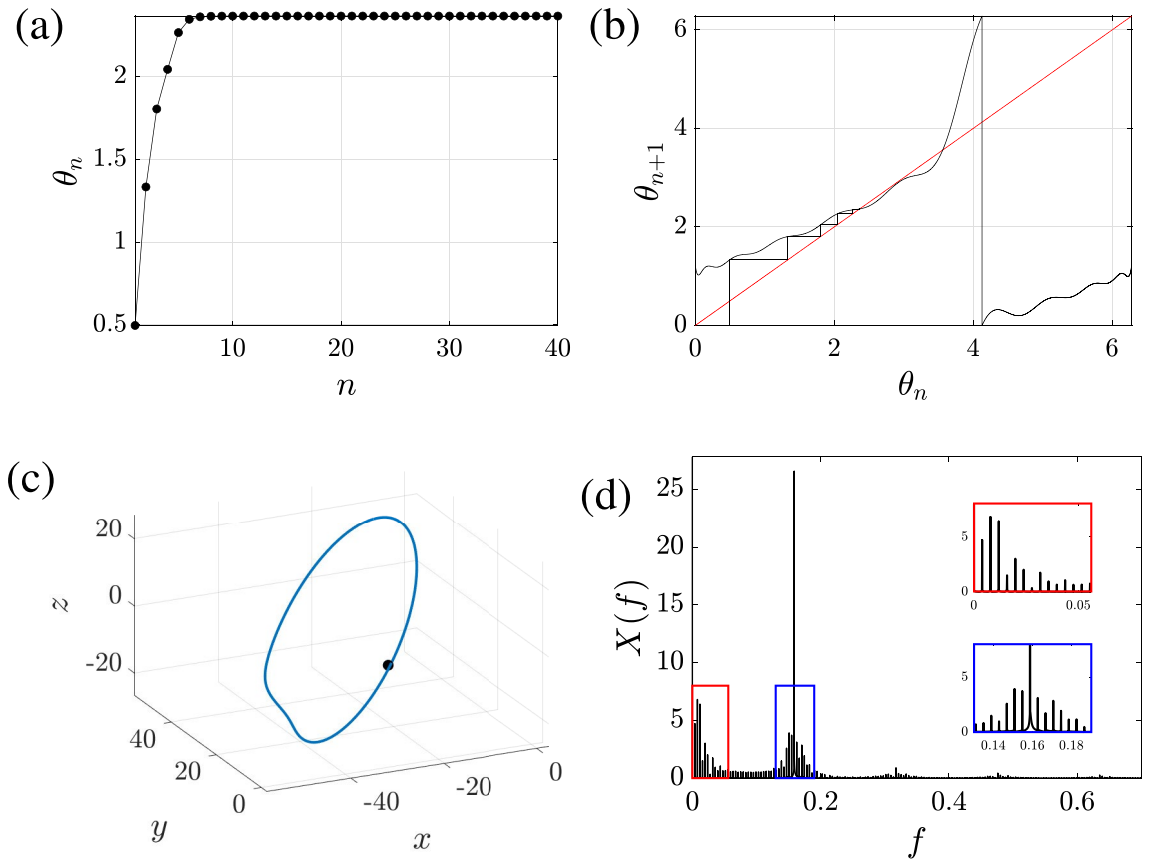


Fig. 9. (a) Circle map orbit, and (b) corresponding cobweb plot. (c) Limit cycle and fixed point of the Poincaré map derived from simulation of the original system. (d) Output spectrum $X(f) = |\mathcal{F}(x(t))|$. The frequency spacing equals $1/(k + s)T$. Forcing parameters: $A = 75, s = 0.1, k = 60$. 1 : 1 cycle. Circuit parameters: $\log_{10} g = 1.18, \log_{10} Q = 1.44, K = 0.5$.

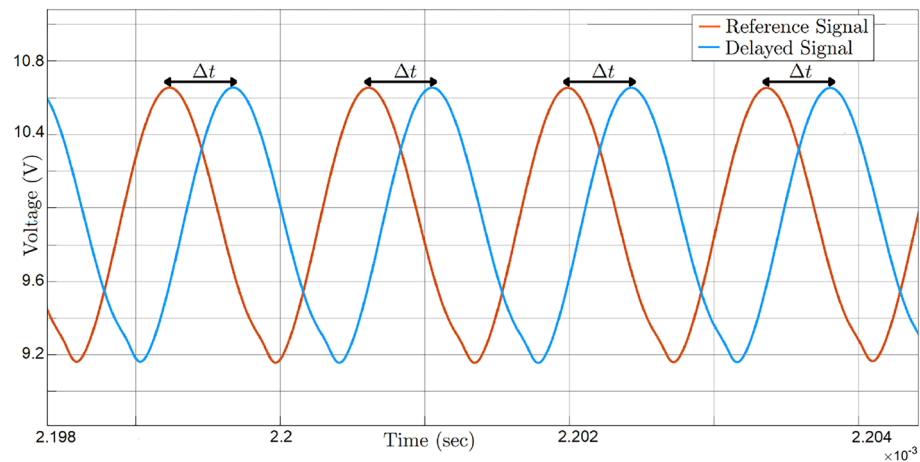


Fig. 10. Time series of the voltages v_{C1} in oscilloscope. Time difference $\Delta t = 0.32T = 440$ ns. Measurement error 1.12 ps.

under the presence of noise, as well as small frequency variations between the oscillators, without necessitating reference to external high-accuracy clocks. The aforementioned features suggest an efficient time and distance measuring mechanism that can be appropriately tuned to a wide variety of timing and positioning applications, under judicious design and parameter selection.

Statistic	Absolute Time Error (ps)	Absolute Distance Error (mm)	Relative Error
Maximum Value	1.12	0.33	8×10^{-6}
Minimum Value	5×10^{-6}	2×10^{-6}	4×10^{-11}
Mean Value	0.43	0.13	3.1×10^{-6}
Std	0.37	0.11	2.7×10^{-6}

Table 3. Time delay and distance error over ten measurements using the synchronized oscillator.

Conclusion

We propose a novel method for high-precision timing and positioning, based on the phase response and the synchronization dynamics of driven nonlinear electronic oscillators. Such oscillators, supporting self-sustained oscillations and serving as clocks, are uniquely characterized by their phase response under an external stimulus enabling their operation as time sensors. Their phase response depends crucially on the characteristic isochron structure of the underlying limit cycle and determines conditions for phase-locking to a received periodic pulse sequence. Under such conditions for a number of identical oscillators located at different positions, each oscillator is locked to a constant phase difference with respect to its received input signal, enabling the precise measurement of the differential time delay between a signal emitted from a source, and therefore precise positioning. The proposed method, presented for archetypical as well as practical electronic circuits, such as Colpitts, is shown to be robust, precise and applicable to any type of electronic oscillator.

Data availability

All data generated or analysed during this study are included in this published article.

Received: 27 February 2025; Accepted: 27 May 2025

Published online: 01 July 2025

References

- Galison, P. *Einstein's Clocks, Poincaré's Maps. Empires of Time* (W.W. Norton & Company, 2004).
- Poincaré, H. The measure of time. In *The Foundations of Science (Translated by G.B. Halsted)*. 223–234 (2015).
- Liu, Q. et al. Management of positioning functions in cellular networks for time-sensitive transportation applications. *IEEE Trans. Intell. Transport. Syst.* **24**, 13260–13275. <https://doi.org/10.1109/TVT.2023.3234532> (2023).
- Angrisano, A., Ascione, S., Cappello, G., Gioia, C. & Gaglione, S. Application of “Galileo high accuracy service” on single-point positioning. *Sensors* **23**. <https://doi.org/10.3390/s23094223> (2023).
- Siraj, M. S., Rahman, A. B., Charatsaris, P., Tsiropoulou, E. E. & Papavassiliou, S. Positioning, navigation, and timing on the air. In *2023 19th International Conference on Distributed Computing in Smart Systems and the Internet of Things (DCOSS-IoT)*. 661–668. <https://doi.org/10.1109/DCOSS-IoT58021.2023.00105> (2023).
- Kaplan, E. D. & Hegarty, C. J. Understanding GPS/GNSS: Principles and applications. In *IEEE Press Series on Aerospace and Electronic Systems* (2017).
- Famili, A., Stavrou, A., Wang, H. & Park, J.-M. Pilot: High-precision indoor localization for autonomous drones. *IEEE Trans. Veh. Technol.* **72**, 6445–6459. <https://doi.org/10.1109/TVT.2022.3229628> (2023).
- Jurdi, R. et al. WhereArtThou: A WiFi-RTT-based indoor positioning system. *IEEE Access* **12**, 41084–41101. <https://doi.org/10.1109/ACCESS.2024.3377237> (2024).
- Kaviani, S., O'Brien, M., Van Brummelen, J., Najjaran, H. & Michelson, D. INS/GPS localization for reliable cooperative driving. In *2016 IEEE Canadian Conference on Electrical and Computer Engineering (CCECE)*. 1–4. <https://doi.org/10.1109/CCECE.2016.7726750> (2016).
- Goncalves Ferreira, A. F. G., Fernandes, D. M. A., Catarino, A. P. & Monteiro, J. L. Localization and positioning systems for emergency responders: A survey. *IEEE Commun. Surv. Tutor.* **19**, 2836–2870. <https://doi.org/10.1109/COMST.2017.2703620> (2017).
- Lee, C. K. M., Ip, C. M., Park, T. & Chung, S. A bluetooth location-based indoor positioning system for asset tracking in warehouse. In *2019 IEEE International Conference on Industrial Engineering and Engineering Management (IEEM)*. 1408–1412. <https://doi.org/10.1109/IEEM44572.2019.8978639> (2019).
- Famili, A., Atalay, T. O., Stavrou, A., Wang, H. & Park, J.-M. OFDRA: Optimal femtocell deployment for accurate indoor positioning of RIS-mounted AVs. *IEEE J. Sel. Areas Commun.* **41**, 3783–3798. <https://doi.org/10.1109/JSAC.2023.3322821> (2023).
- Famili, A., Atalay, T., Stavrou, A. & Wang, H. Wi-Six: Precise positioning in the metaverse via optimal Wi-Fi router deployment in 6G networks. In *2023 IEEE International Conference on Metaverse Computing, Networking and Applications (MetaCom)*. 17–24. <https://doi.org/10.1109/MetaCom57706.2023.00019> (2023).
- Alkendi, Y., Seneviratne, L. & Zweiri, Y. State of the art in vision-based localization techniques for autonomous navigation systems. *IEEE Access* **9**, 76847–76874. <https://doi.org/10.1109/ACCESS.2021.3082778> (2021).
- Groves, P. D. *Principles of GNSS, Inertial, and Multi-Sensor Integrated Navigation Systems* (Artech House, 2013).
- Hong, B. & Hajimiri, A. A general theory of injection locking and pulling in electrical oscillators-Part I: Time-synchronous modeling and injection waveform design. *IEEE J. Solid-State Circuits* **54**, 2109–2121 (2019).
- Buonomo, A., Kennedy, M. P. & Schiavo, A. L. On the synchronization condition for superharmonic coupled QVCOs. *IEEE Trans. Circuits Syst. I Regul. Pap.* **58**, 1637–1646 (2011).
- Buonomo, A. & Lo Schiavo, A. A deep investigation of the synchronization mechanisms in LC-CMOS frequency dividers. *IEEE Trans. Circuits Syst. I Regul. Pap.* **60**, 2857–2866 (2013).
- Buonomo, A. & Lo Schiavo, A. Nonlinear dynamics of divide-by-two injection-locked frequency dividers in locked operation mode. *Int. J. Circuit Theory Appl.* **42**, 794–807 (2014).
- Hong, B. & Hajimiri, A. A general theory of injection locking and pulling in electrical oscillators-Part II: Amplitude modulation in LC oscillators, transient behavior, and frequency division. *IEEE J. Solid-State Circuits* **54**, 2122–2139 (2019).
- Maffezzoni, P. Synchronization analysis of two weakly coupled oscillators through a PPV macromodel. *IEEE Trans. Circuits Syst. I Regul. Pap.* **57**, 654–663. <https://doi.org/10.1109/TCSI.2009.2025000> (2010).

22. Maffezzoni, P. Analysis of oscillator injection locking through phase-domain impulse-response. *IEEE Trans. Circuits Syst. I Regul. Pap.* **55**, 1297–1305 (2008).
23. Gazier, J. & Libchaber, A. Quasi-periodicity and dynamical systems: An experimentalist's view. *IEEE Trans. Circuits Syst.* **35**, 790–809. <https://doi.org/10.1109/31.1826> (1988).
24. Suvak, O. & Demir, A. Quadratic approximations for the isochrons of oscillators: A general theory, advanced numerical methods, and accurate phase computations. *IEEE Trans. Comput.-Aided Des. Integr. Circuits Syst.* **29**, 1215–1228 (2010).
25. Suvak, O. & Demir, A. On phase models for oscillators. *IEEE Trans. Comput.-Aided Des. Integr. Circuits Syst.* **30**, 972–985 (2011).
26. Kennedy, M., Krieg, K. & Chua, L. The devil's staircase: the electrical engineer's fractal. *IEEE Trans. Circuits Syst.* **36**, 1113–1139. <https://doi.org/10.1109/31.192428> (1989).
27. Himona, G., Kovanis, V. & Kominis, Y. Isochrons, phase response and synchronization dynamics of tunable photonic oscillators. *Phys. Rev. Res.* **4**, L012039 (2022).
28. Himona, G., Kovanis, V. & Kominis, Y. Time crystals transforming frequency combs in tunable photonic oscillators. *Chaos Interdiscip. J. Nonlinear Sci.* **33**, 043134 (2023).
29. Famili, A., Himona, G., Kominis, Y., Stavrou, A. & Kovanis, V. Leveraging isochrons of nonlinear oscillators for high-precision localization. *IEEE Internet Things J.* 1–1. <https://doi.org/10.1109/JIOT.2024.3508548> (2024).
30. Himona, G., Famili, A., Stavrou, A., Kovanis, V. & Kominis, Y. Isochrons in tunable photonic oscillators and applications in precise positioning. In *Physics and Simulation of Optoelectronic Devices XXXI*. Vol. 12415. 82–86 (SPIE, 2023).
31. Famili, A., Himona, G., Kominis, Y., Stavrou, A. & Kovanis, V. Isochrons in injection locked photonic oscillators: A new frontier for high-precision localization. *IEEE J. Indoor Seamless Position. Navig.* 1–16. <https://doi.org/10.1109/JISPIN.2024.3504396> (2024).
32. Winfree, A. T. *The Geometry of Biological Time* (Springer, 1980).
33. Pavlidis, T. *Biological Oscillators: Their Mathematical Analysis* (Academic Press, 1973).
34. Izhikevich, E. M. *Dynamical Systems in Neuroscience: The Geometry of Excitability and Bursting* (MIT Press, 2007).
35. Ermentrout, G. B. & Terman, D. H. *Mathematical Foundations of Neuroscience* (Springer, 2010).
36. Wedgwood, K. C., Lin, K. K., Thul, R. & Coombes, S. Phase-amplitude descriptions of neural oscillator models. *The Journal of Mathematical Neuroscience* **3**, 1–22 (2013).
37. Guckenheimer, J. & Holmes, P. *Nonlinear oscillations, dynamical systems, and bifurcations of vector fields* (Springer, 1983).
38. Strogatz, S. H. *Nonlinear Dynamics and Chaos: With Applications to Physics, Biology, Chemistry, and Engineering* (CRC Press, 2015).
39. Kuznetsov, Y. A. *Elements of Applied Bifurcation Theory* (Springer, 2004).
40. der Pol, B. V. A theory of the amplitude of free and forced triode vibrations. *Radio Review* **1**(701–710), 754–762 (1920).
41. Guckenheimer, J. Isochrons and phaseless sets. *J. Math. Biology* **1**, 259–273 (1975).
42. Monga, B., Wilson, D., Matchen, T. & Moehlis, J. Phase reduction and phase-based optimal control for biological systems: a tutorial. *Biological cybernetics* **113**, 11–46 (2019).
43. Pikovsky, A., Rosenblum, M. & Kurths, J. *Synchronization: A Universal Concept in Nonlinear Sciences* (Cambridge University Press, 2001).
44. Glass, L. & Perez, R. Fine structure of phase locking. *Phys. Rev. Lett.* **48**, 1772–1778 (1982).
45. Glass, L. & Sun, J. Periodic forcing of a limit-cycle oscillator: Fixed points, arnold tongues, and the global organization of bifurcations. *Phys. Rev. E* **50**, 5077 (1994).
46. Langfield, P., Facanhay, W. L. C., Oldeman, B. & Glass, L. Bifurcations in a periodically stimulated limit cycle oscillator with finite relaxation times. *SIAM J. Appl. Dyn. Systems* **16**, 1045–1069 (2017).
47. The MathWorks, Inc. Simscape Electrical (2024). Online Accessed Dec 2024.
48. Maggio, G., De Feo, O. & Kennedy, M. Nonlinear analysis of the colpitts oscillator and applications to design. *IEEE Transactions on Circuits and Systems I: Fundamental Theory and Applications* **46**, 1118–1130 (1999).
49. De Feo, O., Maggio, G. & Kennedy, M. The colpitts oscillator: Families of periodic solutions and their bifurcations. *Int. J. Bifur. Chaos* **10**. <https://doi.org/10.1142/S0218127400000670> (2012).
50. Mauroy, A. & Mezić, I. On the use of Fourier averages to compute the global isochrons of (quasi) periodic dynamics. *Chaos Interdiscip. J. Nonlinear Sci.* **22** (2012).
51. Mauroy, A. & Mezić, I. Global computation of phase-amplitude reduction for limit-cycle dynamics. *Chaos Interdiscip. J. Nonlinear Sci.* **28** (2018).
52. Mauroy, A., Susuki, Y. & Mezić, I. *Koopman Operator in Systems and Control* (Springer, 2020).

Author contributions

K.M. performed numerical calculations on electronic oscillators. G.H. performed analytical and numerical calculations on standard limit-cycle oscillators. G.H., A.F., A.S. and Y.K. conceived the idea of exploiting the phase response and the synchronization dynamics of oscillators for precise timing and positioning. All authors reviewed the manuscript.

Declarations

Competing interests

The authors declare no competing interests.

Additional information

Correspondence and requests for materials should be addressed to A.S. or Y.K.

Reprints and permissions information is available at www.nature.com/reprints.

Publisher's note Springer Nature remains neutral with regard to jurisdictional claims in published maps and institutional affiliations.

Open Access This article is licensed under a Creative Commons Attribution-NonCommercial-NoDerivatives 4.0 International License, which permits any non-commercial use, sharing, distribution and reproduction in any medium or format, as long as you give appropriate credit to the original author(s) and the source, provide a link to the Creative Commons licence, and indicate if you modified the licensed material. You do not have permission under this licence to share adapted material derived from this article or parts of it. The images or other third party material in this article are included in the article's Creative Commons licence, unless indicated otherwise in a credit line to the material. If material is not included in the article's Creative Commons licence and your intended use is not permitted by statutory regulation or exceeds the permitted use, you will need to obtain permission directly from the copyright holder. To view a copy of this licence, visit <http://creativecommons.org/licenses/by-nc-nd/4.0/>.

© The Author(s) 2025